INL/JOU-17-42347-Revision-0

SEM characterization of two advanced fuel alloys: U-10Zr-4.3Sn and U-10Zr-4.3Sn-4.7Ln

Michael T. Benson, James A. King, Robert D. Mariani, M Craig Marshall

October 2017

The INL is a U.S. Department of Energy National Laboratory
operated by Battelle Energy Alliance

INL/JOU-17-42347-Revision-0

SEM characterization of two advanced fuel alloys: U-10Zr-4.3Sn and U-10Zr-4.3Sn-4.7Ln

Michael T. Benson, James A. King, Robert D. Mariani, M Craig Marshall

October 2017

Idaho National Laboratory
Idaho Falls, Idaho 83415

http://www.inl.gov

Prepared for the
U.S. Department of Energy

Under DOE Idaho Operations Office
Contract DE-AC07-05ID14517

SEM characterization of two advanced fuel alloys: U-10Zr-4.3Sn and U-10Zr-4.3Sn-4.7Ln

Michael T. Benson, James A. King, Robert D. Mariani, M. Craig Marshall

Idaho National Laboratory, P.O. Box 1625, MS 6188, Idaho Falls, ID 83415

Corresponding Author Information
Michael T. Benson, phone: (208) 533-8870, FAX: (208) 533-7863, email: michael.benson@inl.gov

Submitted to Journal of Nuclear Materials
June 2017

SEM characterization of two advanced fuel alloys: U-10Zr-4.3Sn and U-10Zr-4.3Sn-4.7Ln

Michael T. Benson, James A. King, Robert D. Mariani, M. Craig Marshall

Idaho National Laboratory, P.O. Box 1625, MS 6188, Idaho Falls, ID 83415

Abstract

Tin is being investigated as a potential additive to metallic fuel to control fuel-cladding chemical interaction (FCCI). A primary cause of FCCI is the lanthanide fission products moving to the fuel periphery and interacting with the cladding. This interaction will lead to wastage of the cladding and eventually to a cladding breach. The current study is a scanning electron microscopy (SEM) characterization of as-cast and annealed U-10Zr-4.3Sn and U-10Zr-4.3Sn-4.7Ln, where Ln=53Nd-25Ce-16Pr-6La. The present study shows that tin preferentially binds the lanthanides, which will prevent lanthanide migration and interaction with the cladding.

Keywords

metallic fuel, FCCI, fuel additive

1. Introduction

Fuel-cladding chemical interaction (FCCI) occurs when the nuclear fuel or fission products react with the cladding material. A major cause of FCCI in metallic fuels during irradiation is fission product lanthanides (Ln), which tend to migrate to the fuel periphery, coming in contact with the cladding. The result of this interaction is degradation of the cladding, and will eventually lead to rupture of the fuel assembly [1][2]. In order to extend fuel life, while making the fuel less likely to have a cladding breach, some method of controlling FCCI is needed. Several methods are being investigated to decrease or prevent FCCI, such as barrier foils, coatings, and additive materials [3][4][5][6]. In the additive approach, considering ways to bind

lanthanides as stable intermetallics, criteria were developed that identified a set of elements that could be promising additives [3]. From this list, Pd [3][7][8] and In [6] have been investigated, and have both shown promise as a fuel additive.

The lanthanides can burn-in as fission products, or can be present in fuel produced with recycled uranium. A small amount of lanthanides are expected to remain with uranium after pyroprocessing, thus being incorporated into a fresh fuel [9]. In this case, as soon as the fuel contacts the cladding due to swelling, at roughly 1-2% burnup, there are already lanthanide impurities in the recycled fuel available to initiate FCCI. This early form of FCCI in a recycled fuel will occur in accelerated fashion in comparison to the much slower burn-in of fission product lanthanides in a fresh fuel fabricated with clean uranium. Controlling FCCI in this system is even more important due to the potentially reduced lifetime of the fuel [10].

The current study is the initial investigation using Sn as a fuel additive. There are multiple reports of Sn-U interactions, due to Sn being a minor component in Zr-based cladding [11][12][13] and also for the molten Sn process for reprocessing oxide and carbide fuels [14][15]. Tin was previously identified as a potential fuel additive [3], but to date has not been investigated as such. The current study examines U-Zr alloys with Sn and with both Sn and a mix of lanthanides. The composition and ratio of lanthanides are based on elemental analysis of irradiated U-10Zr EBR-II fuel pins [3], with the four most prevalent lanthanides included in the mix. The ratio obtained from EBR-II fuel is 53Nd-25Ce-16Pr-6La, in wt %. In the case of recycled fuel, the starting concentrations of lanthanides will have a slightly different elemental ratio; the ratio of lanthanides in recycled fuel will be modified slightly from their fission product yields by the separation factors in the pyrometallurgical process.

Pure Sn has a melting point (232°C) roughly 400°C below operating fuel temperatures, around 650°C. Free Sn could be highly detrimental to the fuel, with respect to possible unknown fission product transport issues or to possible liquid metal embrittlement of the cladding. Ruling out these concerns, along with investigating the as-cast and annealed microstructures is the motivation for this out-of-pile, separate-effects testing reported here.

2. Experimental methods

Two alloys were cast, U-10Zr-4.3Sn wt% (71.2U-21.7Zr-7.2Sn at%) and U-10Zr-4.3Sn-4.7Ln (65.4U-21.1Zr-7.0Sn-6.5Ln at%), where Ln = 53Nd-25Ce-16Pr-6La wt% (52.3Nd-25.4Ce-16.2Pr-6.1La at%). All materials, except uranium, were obtained from Alfa Aesar and used as received. The lanthanides were obtained as rods, packaged in mylar under argon. Uranium was cleaned by submersion in nitric acid, followed by a water wash, then an ethanol wash.

All casting operations were carried out in an arc-melter within an argon atmosphere glovebox with high purity argon as a cover gas. After each addition step, the resulting button was flipped and re-melted 3 times to ensure homogeneity. To prepare U-10Zr-4.3Sn, the appropriate amount of Sn, Zr, and U were arc melted together in two steps. A button was prepared of U-Zr, followed by addition of Sn. To prepare 53Nd-25Ce-16Pr-6La, the appropriate amount of each lanthanide was arc melted together in one step. To prepare U-10Zr-4.3Sn-4.7Ln, the appropriate amount of the Ln alloy was added to a button of U-Zr-Sn, prepared as described for U-10Zr-4.3Sn. The buttons were cast into 5mm diameter pins.

Approximately 4mm from each pin was cut for annealing. The samples were wrapped in Ta foil, then sealed in quartz tubes under vacuum. The quartz tube was placed in a furnace at 650°C

for 500 hours. After the heat treatment, the samples were quenched in water. The samples were cut to expose a fresh surface for analysis.

Scanning electron microscopy (SEM) was performed on a section of pin from each alloy for both as-cast and annealed. The samples were mounted in a 31.8 mm diameter phenolic metallographic (met) mount filled with epoxy. Samples were polished by grinding the surfaces flat with SiC grinding paper followed by polishing with polycrystalline diamond suspensions, starting with 9μm, then 3 μm, and finally 1 μm. The polished samples were analyzed with a sputtered coating of approximately 15nm carbon to control charging of the metallographic mount.

The instrument used for this analysis was a JSM-7600f scanning electron microscope (SEM) manufactured by the Japan Electron Optics Laboratory (JEOL). The JSM-7600f is a hot field emission SEM equipped with an Oxford Instruments X-Max 20 silicon drift energy dispersive X-ray spectrometer (EDS). The X-ray spectrometer is controlled by Oxford INCA software (v. 4.15, part of the Oxford Microanalysis Suite Issue 18d + SP 4), which also provides image acquisition capabilities.

The SEM was operated at an accelerating voltage of 20kV and a nominal beam current of approximately 84nA (which can vary somewhat with column conditions) for these analyses. Prior to analysis, X-ray detector response was verified using a copper target. All of the X-ray spectra were accumulated for 75 live seconds. Spectra were collected over the energy range 0 – 20keV, which covers characteristic X-ray energies from all analytes.

Spectra were quantified using so-called “standardless” analysis, which uses a stored library of reference spectra to quantify unknown spectra rather than physical standards. This method is

generally accurate to the 0.1 to 0.5 wt/wt% range, depending on sample and microscope (observation) conditions.

Phase transformation temperatures for U-10Zr-4Sn were measured using a Netzsch DSC 404C Differential Scanning Calorimeter (DSC). The sample was held in an alumina lined Pt-Rh crucible, with ultra-high purity argon as the cover gas at a flow rate of 50 mL/min after passing it through an Oxy-gon OG-120M oxygen gettering furnace. Oxygen impurity levels were in the sub ppb range based on the measured performance of the gettering furnace. The DSC was programmed to ramp to the target temperature of 1500°C at a rate of 10 °C/min, holding at temperature for 10 minutes, then cooling to room temperature (also at 10 °C/min).

3. Results and discussion

Tin has a low melting point (231.9°C), but a high boiling point (2,603°C) with a relatively low vapor pressure at fuel processing and operating temperatures. There were no difficulties casting buttons and pins with Sn, and no apparent loss while casting. Multiple intermetallic compounds are possible between Sn with Zr and U, thus there is no loss of Sn, and should be no free Sn in the alloy.

Throughout this manuscript, specific phases are discussed. Phases in a U-Zr alloy, α-U and δ phase, have been characterized and are known [16]. Phases including Sn and/or lanthanides are inferred from EDS results. Crystallography is underway to confirm the phases, but is not included in this study.

3.1 U-10Zr-4.3Sn

Alloy U-10Zr-4.3Sn (wt%) represents a possible advanced fresh fuel alloy composition. The concentration of Sn was chosen based on a previous investigation using Pd as a fuel additive [3]. In that study, the highest Pd content, 3.86 wt%, was chosen to bind the lanthanides produced at roughly 20% burnup in a 1:1 compound. This concentration was used for Sn to keep continuity in the ongoing fuel additive research at Idaho National Laboratory.

SEM images, using backscattered electrons (BSE), of as-cast U-10Zr-4.3Sn are shown in Figure 1a and 1b. The outer region of the pin cross-section is shown in Figure 1a. The triangular dendritic structures were found to a depth of roughly 500 μm. At greater depths, the hexagonal structures shown in Figure 1b are the only remaining precipitates. The hexagonal precipitates and the triangular dendrites, shown in Figure 1a, are shown with a higher magnification in Figure 2, with accompanying EDS data listed in Table 1. A higher magnification view from Figure 1b, showing the hexagonal precipitates, is shown in Figure 3, with EDS data listed in Table 2.

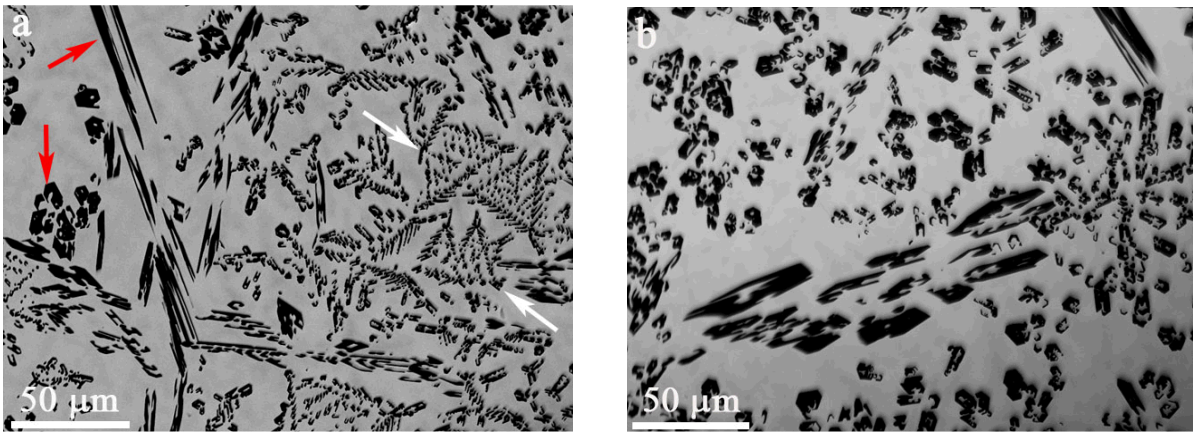

Figure 1. SEM BSE image for as-cast U-10Zr-4.3Sn. a. outer region of pin showing both hexagonal (red arrows) and triangular dendritic (white arrows) precipitates; b. central region of pin showing only hexagonal precipitates.

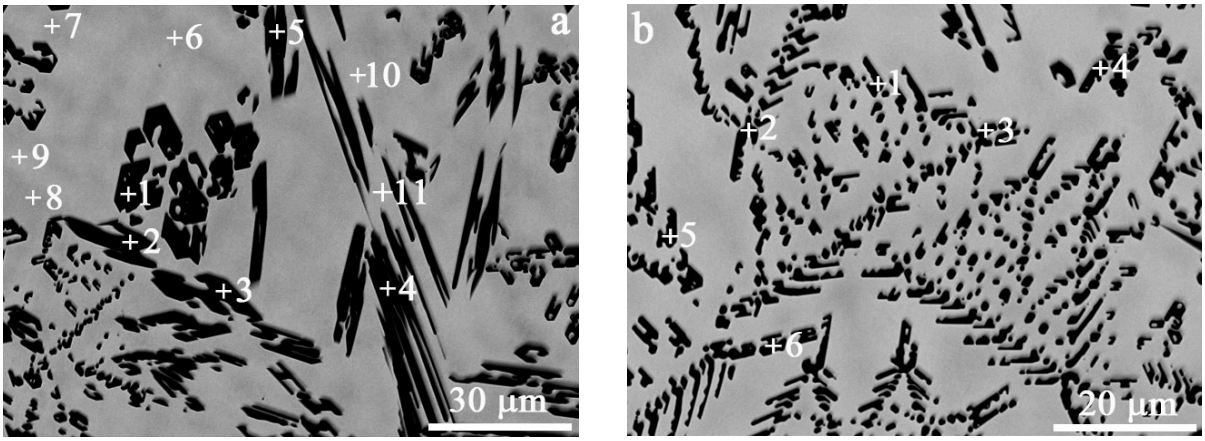

Figure 2. Higher magnification views of the image shown in Figure 1a. a. hexagonal precipitates, b. triangular dendrites. EDS data listed in Table 1.

Table 1. EDS data for points shown in Figure 2. Values in atomic %.

	U	Zr	Sn
Figure 2a			
1	1.9	61.5	36.6
2	2.8	61.1	36.1
3	2.4	61.1	36.5
4	2.9	61.2	35.9
5	2.3	61.2	36.5
6	80.8	17.8	1.4
7	81.5	17.0	1.5
8	81.6	16.7	1.7
9	88.7	10.1	1.2
10	88.2	10.7	1.1
11	87.4	11.3	1.4
Figure 2b			
1	10.1	56.6	33.3
2	10.6	57.1	32.3
3	9.6	57.3	33.1
4	9.3	57.4	33.3
5	6.3	59.5	34.3
6	8.2	58.1	33.6

The Zr/Sn ratio in the black precipitates varies only slightly for each set of data. The average ratio for the points shown in Figure 2a is 1.68, for Figure 2b it is 1.73, and for Figure 3 it is 1.62. These ratios are all practically the same, within experimental error for EDS. The data for Figure 2b is likely less reliable. Due to the small size of the precipitates, a significant amount of the surrounding matrix (in Figure 2b) was detected during analysis.

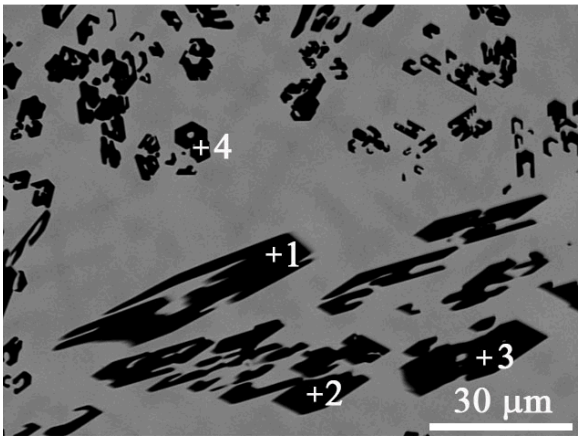

Figure 3. Higher magnification view of the image shown in Figure 1b. EDS data listed in Table 2.

Table 2. EDS data for points shown in Figure 3. Values in atomic %.

	U	Zr	Sn
1	1.9	60.6	37.5
2	2.0	60.5	37.5
3	2.2	60.3	37.6
4	4.0	59.7	36.3

The binary phase diagram for the Zr-Sn system is shown in Figure 4 [17]. For the Zr-Sn ratios that were observed (Tables 1 and 2), the relevant region is at a Sn concentration of 40 at %, with a composition of Zr_5Sn_3. This ratio appears consistent across the entire pin, although the precipitates at the outer region of the pin have a dendritic morphology compared to the hexagonal morphology predominating at the inner region of the pin. The hexagonal structure is visible in some of the larger areas at the points of the triangles, indicating the composition is likely the same throughout the precipitates. The visual differences are likely due to the rapid cooling at the periphery during the pin casting process, with the inner region cooling slower, allowing formation of the larger hexagonal structures.

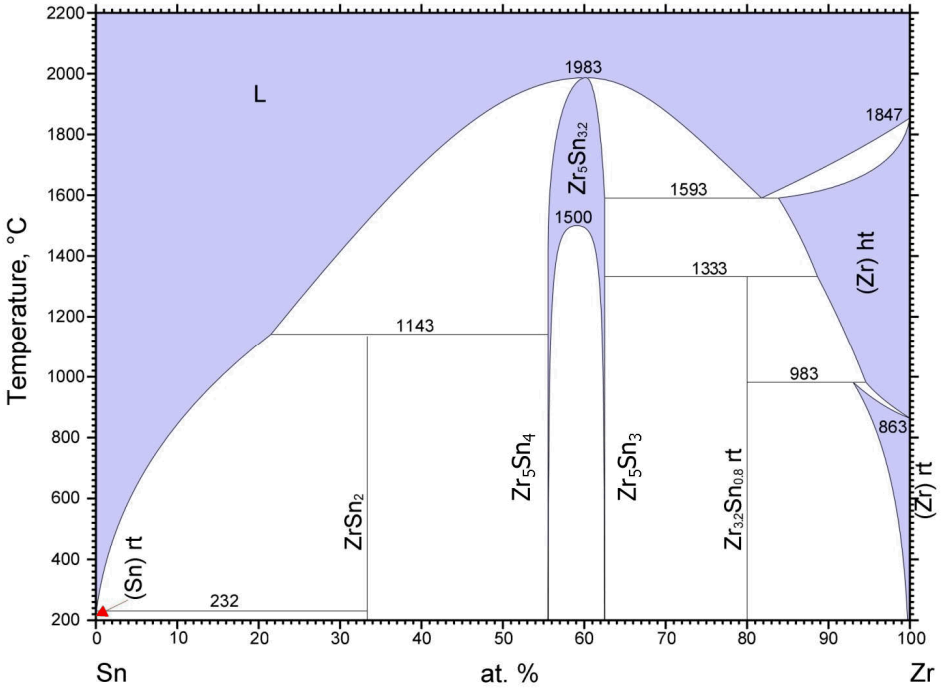

Figure 4. Zr-Sn binary phase diagram [17], with added annotations for Zr_5Sn_4 and Zr_5Sn_3.

The starting concentration in the alloy, 71.2U-21.7Zr-7.2Sn at%, corresponds to a normalized Zr-Sn ratio of 75.2Zr-24.8Sn at%. This ratio is not observed in the precipitates, though, due to some Zr remaining in the uranium matrix. EDS data listed for the points shown in Figures 2a indicates the Zr content varies from roughly 10.1 to 17.8 at% in the matrix. As observed in U-Zr alloys[18], there is a differentiation in the matrix, with lighter (low Zr) and darker (higher Zr) regions visible.

Figure 5 shows images for U-10Zr-4.3Sn after annealing at 650°C for 500 hours. Figure 5b is an increased magnification view of the inner pin region shown in Figure 5a, with EDS analysis points shown. EDS data is listed in Table 3. There is no noticeable change in the precipitates, along the outer region of the pin (not shown) or the inner region. The Zr/Sn ratio is roughly 1.68, indicating the composition is still Zr_5Sn_3. A change in either the appearance or

composition of the precipitates was not expected given the high decomposition temperature for Zr_5Sn_3.

Upon annealing the matrix resolves into α-U and δ phase, evident by the light and dark regions present in the matrix. The U content in the δ phase, Table 3, points 1-3, is high, but the analyzed points are very small in size, so U from the surrounding α-U regions is included in the analysis. The amount of δ phase present is small, due to Zr being consumed in the Zr-Sn precipitates.

There is a small amount of Sn present in the U-rich regions before and after annealing (Table 1, points 9-11, and Table 3, points 4-6). The amount of Sn is very small, though, less than 2 at%. U_5Sn_4 is a possible intermetallic in the U-Sn system [19], but there is no EDS evidence to suggest an intermetallic is forming. Based on these observations, Sn clearly has a preference to bind to Zr in this fresh fuel composition. The small amount of Sn present in the U-rich regions could possibly arise from slightly enhanced solid solubility of Sn that derives from the presence of Zr in these regions.

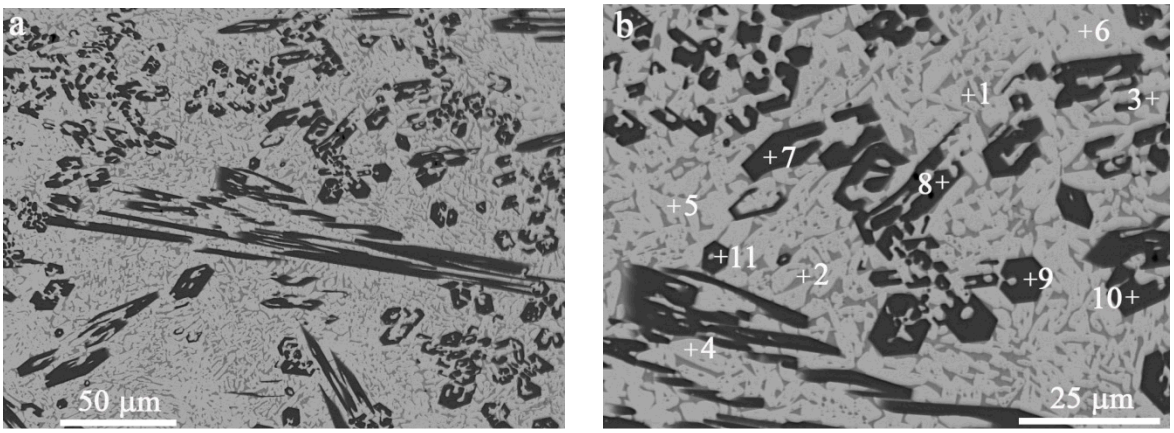

Figure 5. SEM BSE images for annealed U-10Zr-4Sn. a. central region of pin; b. higher magnification view showing EDS points. EDS data listed in Table 3.

Table 3. EDS data for points shown in Figure 5b. Values in atomic %.

	U	Zr	Sn
1	38.7	60.8	0.5
2	39.1	60.1	0.7
3	39.3	60.5	0.3
4	97.8	0.8	1.4
5	97.6	1.2	1.2
6	96.9	1.3	1.8
7	2.0	61.5	36.6
8	1.9	61.6	36.5
9	2.0	61.5	36.5
10	1.9	61.3	36.8
11	2.1	61.2	36.7

The measured Zr/Sn ratio is very close to Zr_5Sn_3, with the small differences likely due to limitations in the method. The starting concentration of Sn in the alloy is 7.2 at%, which will require 12.0 at% Zr to completely consume the available Sn in forming Zr_5Sn_3, leaving 10.5 at% Zr for the matrix. For this concentration of Zr, the solidus temperature should be roughly 1175°C, based on the U-Zr phase diagram [20].

Differential Scanning Calorimetry (DSC) results for the as-cast alloy, shown in Fig. 6, indicate a solidus of 1192°C which corresponds closely to the solidus estimated from the EDS results. DSC data are summarized in Table 4. Given this solidus temperature, the actual concentration of Zr in the matrix should be between 12 and 12.5 at%. This small difference in composition (10.5 compared to 12 at%) is close to the error inherent in EDS, and could also be accounted for in terms of the small amount of Sn observed by SEM in the matrix. A small amount of Sn in the matrix would yield less Zr_5Sn_3, and therefore a slightly higher Zr content available in the matrix to produce a slightly higher solidus as observed in the DSC. This simple analysis is based on the starting weights of the materials, though, and does not take into account possible losses or inhomogeneities that can arise while arc melting. While high precision wet

chemical analysis of the cast pins was not performed, the casting recipe and DSC results are reasonably consistent with each other.

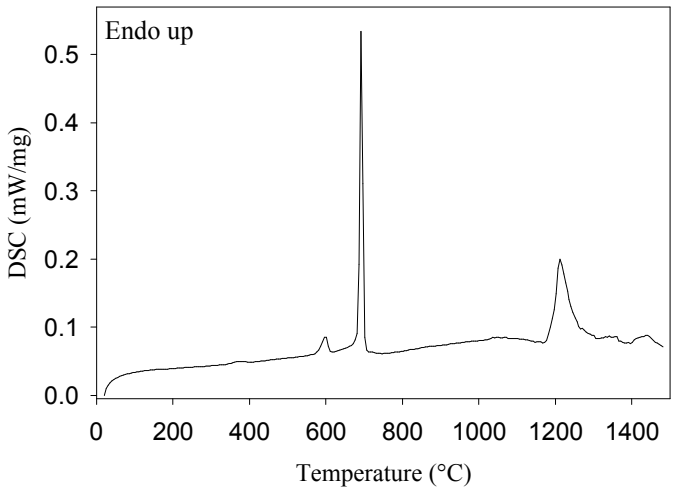

Figure 6. DSC curve for as-cast U-10Zr-4Sn.

Table 4. DSC data for as-cast U-10Zr-4Sn

Peak Start (°C)	Peak (°C)	Peak End (°C)	Transition
578	599	610	$(\alpha,\delta)\rightarrow(\alpha,\gamma_2)$
685	693	700	$(\alpha,\gamma_2)\rightarrow(\alpha,\gamma_1)$
1192	1211	1256	liquidus

The DSC curve is essentially the same as for a U-Zr alloy, since the Zr-Sn precipitates decompose very close to, or above, the maximum temperature for this DSC. The upper temperature region (>1400°C), above the solidus/liquidus peak, may be the initial decomposition of Zr_5Sn_3. Given that the measured DSC curve does not include contributions from Sn, the peak assignments are based on the U-Zr phase diagram [20][21].

The decrease in Zr content in the matrix due to precipitate formation is important in the performance of a metallic fuel. The primary reason for adding Zr is to raise the solidus/liquidus temperatures, especially in the case of a transmutation fuel, due to the significant drop in solidus

temperature upon addition of Pu [22]. To negate this drop, extra Zr will have to be added. Additions of non-fissile material to the fuel need to be kept at a minimum, though, in order to maintain fuel performance. The other fuel additives investigated, Pd and In, also deplete Zr from the matrix. Pd forms $PdZr_2$ [3], while the reported Zr/In ratio of 2.5 corresponds to Zr_5In_2 [6]. Of the additives investigated to date, Sn has the most advantageous Zr/Sn ratio (1.67), depleting the least amount of Zr from the matrix.

Surprisingly, no α-Zr precipitates were found in the alloy, before or after annealing, although it is commonly found in U-Zr alloys, with or without additives [3][23]. Based on the phase diagram [20], it should not exist, and is believed to be caused by small amounts of oxygen having a stabilizing effect on α-Zr [23]. The same U and Zr feedstocks and polishing procedures were used as for previous U-10Zr alloys and U-Zr-Pd alloys, all of which contained α-Zr precipitates. This indicates the lack of α-Zr in the U-Zr-Sn alloy is not due to fabrication or sample preparation. Since no additional steps were taken to exclude oxygen, the small amounts of oxygen are still present, and are likely associated with the Zr-Sn precipitates.

In both the as-cast and annealed microstructures, no precipitates of isolated Sn were observed. While expected from the phase diagrams, this result is important and favorable to demonstrate, because of the low melting point of Sn, and the possibility of liquid-metal embrittlement of the cladding. In this U-Zr-Sn alloy, all of the Sn appears to be bound at these concentrations, even though a small amount (<2 at%) was dissolved in the α-U and δ phases in the annealed structure and in the light and dark regions of the as-cast alloy. Based on the phase diagrams [17][19], there is no solubility of Sn in U, and only a small solubility of Sn in Zr. The low concentration of Sn found could arise from a slight solubility of Sn in the fuel matrix, made favorable by the presence of dissolved Zr, or δ phase. The low concentration of Sn could also be

an artifact of the spot size overlapping nearby Zr-Sn precipitates, or due to a small amount of overlap of the X-rays peaks used in the EDS analysis for Sn and U. Regardless, there is no evidence of any liquid behavior in the annealed sample, ruling out the possibility of free Sn. Furthermore, any enhanced solid solubility of Sn in the fuel matrix that may arise from the presence of Zr indicates a lesser activity of Sn, i.e., its stabilization in the fuel matrix.

3.2 U-10Zr-4.3Sn-4.7Ln

The composition U-10Zr-4.3Sn-4.7Ln (65.4U-21.1Zr-7.0Sn-6.5Ln at%) was chosen to represent a fuel after roughly 16% burnup, similar to previous work with U-Zr-Pd alloys [3], based on lanthanide composition. This composition has a small molar excess of Sn, thus no free lanthanides should be present.

The microstructure of the alloy changes significantly upon addition of lanthanides, as shown in Figure 7. A representative large area BSE image of the alloy is shown in Figure 7a. Figure 7b shows a large precipitate within this alloy, with EDS analysis listed in Table 5. The alloy shows several distinct features. There are rough, random shaped precipitates, round precipitates, and black precipitates that appear to be Zr_5Sn_3, as observed in U-10Zr-4.3Sn. There is a slight molar excess of Sn in the alloy, relative to lanthanide content (65.4U-21.1Zr-7.0Sn-6.5Ln at%), so the presence of some Zr_5Sn_3 was expected. The uranium matrix is similar to that observed in U-10Zr, with light and dark regions, as was also observed for the U-Zr-Sn alloy described in the previous section.

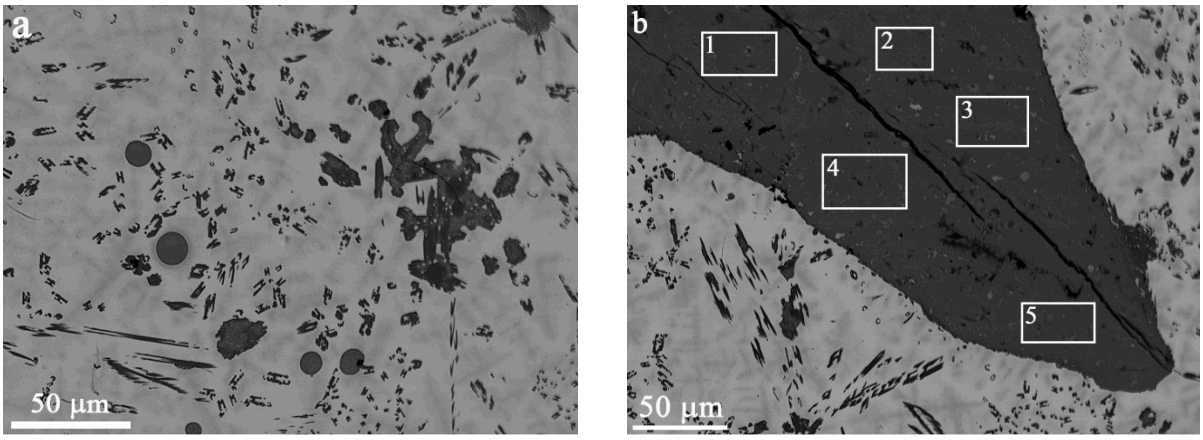

Figure 7. SEM BSE image for as-cast U-10Zr-4.3Sn-4.7Ln. a. representative region of pin; b. large precipitate. EDS data for b listed in Table 5.

Table 5. EDS data for areas shown in Figure 7b. Values in atomic %.

	U	Zr	Sn	Nd	Ce	Pr	La
1	2.0	15.5	32.1	26.1	12.2	8.5	3.6
2	2.1	14.7	32.3	26.2	12.5	8.4	3.8
3	1.8	11.5	34.6	27.3	12.5	8.5	3.8
4	2.0	13.7	32.9	26.4	12.6	8.5	3.9
5	2.0	14.1	33.0	26.1	12.5	8.4	4.0

The sample slice that was cut and analyzed happened to contain the large precipitate region shown in Figure 7b. Other samples cut from the pin did not contain large precipitates. The precipitate extended roughly 2 mm into the pin, and was also present at the periphery. From the EDS data collected, the ratio of lanthanides to Sn is roughly 1.56, putting the composition between Ln_5Sn_3 and Ln_5Sn_4. Given that Nd is the largest component of the lanthanide mix, the densities for Nd_5Sn_3 and Nd_5Sn_4 will be used for this discussion. The density is 7.17 and 7.26 g/cm^3 for Nd_5Sn_3 and Nd_5Sn_4, respectively [24][25], which are significantly lower than the density for U metal, 19.1 g/cm^3. Due to this density difference, it is believed the alloy was completely mixed during arc melting, and the separation occurred during the pin casting process. This separation has been observed in other uranium-additive alloys upon addition of lanthanides [26]. This should not adversely affect the analysis, since the lanthanides are still uniformly

spread throughout the alloy, just in lower concentrations than would be observed if the large precipitate had not separated from the alloy. This result is unlikely to occur in a reactor, though, since the lanthanides will burn-in slowly. This result might be a concern when fuel is fabricated with recycled uranium, because a small amount of lanthanides could separate with Sn, causing an uneven distribution of fissile material throughout the fuel. In recycled fuel, however, with lanthanides present in minor quantities, the added Sn will be present in large excess, and the Sn should aid dispersal of the lanthanides, based on behavior of the U-Zr-Sn without lanthanides.

Increased magnification images from Figure 7a are shown in Figures 8a and 8b, with EDS data listed in Table 6. Analysis of the matrix region (points 1-3 in Figure 8a, Table 6) indicates the dark matrix regions contain significantly more Zr (>30 at%) than found in U-10Zr-4.3Sn (~17 at%). The light matrix regions are roughly the same between the alloys. The alloy was fabricated by adding lanthanides to a pre-alloy of U-Zr-Sn, thus the pre-alloy might be expected to look very similar to U-10Zr-4.3Sn, i.e. with a significant amount of Zr tied up in Zr-Sn precipitates. The increase in Zr content in the dark matrix regions clearly indicates Zr is being released back into the matrix, and that Sn has a preference to bind lanthanides.

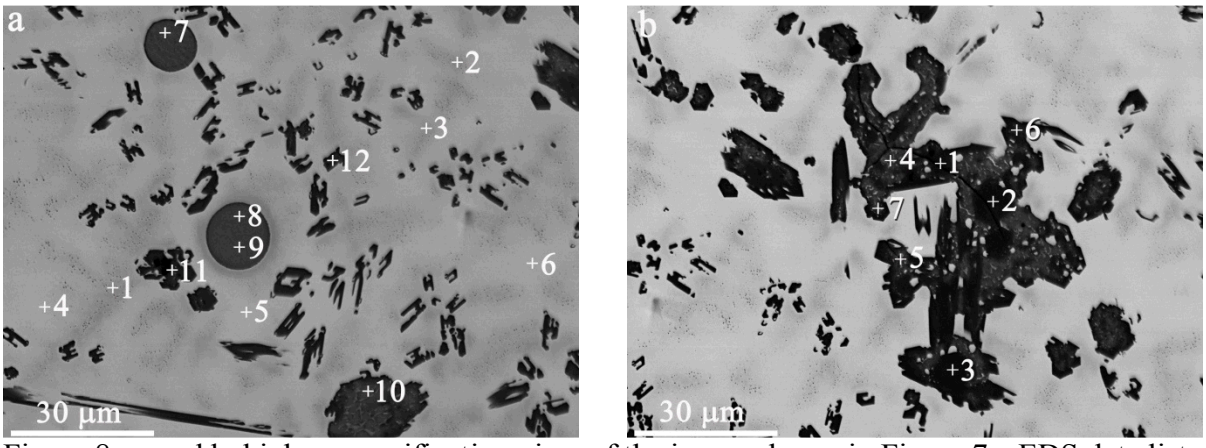

Figure 8. a. and b. higher magnification view of the image shown in Figure 7a. EDS data listed in Table 6.

Table 6. EDS data for points shown in Figure 8. Values in atomic %.

	U	Zr	Sn	Nd	Ce	Pr	La
Figure 8a							
1	65.1	32.9	1.6	0.0	0.2	0.2	0.0
2	61.9	35.5	2.3	0.0	0.3	0.0	0.0
3	67.5	30.3	1.5	0.0	0.4	0.2	0.1
4	86.7	11.5	1.2	0.0	0.2	0.4	0.0
5	88.7	9.4	1.0	0.0	0.5	0.5	0.0
6	89.2	9.0	1.3	0.0	0.3	0.2	0.0
7	2.6	15.9	35.0	22.5	13.4	7.7	2.9
8	1.5	11.8	36.5	23.4	15.6	8.4	2.9
9	1.6	12.0	36.8	23.0	15.5	8.3	2.8
10	4.2	21.5	33.3	20.0	12.0	6.8	2.2
11	1.3	63.4	32.4	2.0	0.4	0.5	0.0
12	3.7	52.9	35.6	4.2	1.8	1.3	0.4
Figure 8b							
1	1.7	59.9	36.6	1.0	0.3	0.3	0.2
2	1.8	61.5	36.5	0.0	0.1	0.0	0.1
3	2.1	61.3	36.5	0.0	0.0	0.0	0.0
4	6.0	15.9	34.2	21.8	10.9	7.2	4.0
5	10.3	15.9	31.5	21.3	10.4	7.0	3.7
6	2.3	23.2	36.1	19.5	9.6	6.0	3.3
7	4.8	22.7	32.8	20.1	9.7	6.6	3.4

The round precipitates (points 7-9 in Figure 8a, Table 6) are very similar in composition to the large precipitate shown in Figure 7b. The rough, random shaped precipitates are a mix of Zr, Sn, and lanthanides, although the composition varies from Zr_5Sn_3 to Ln_5Sn_3 with variable amounts of Zr. These precipitates appear to be frozen during the reaction converting Zr_5Sn_3 to Ln_5Sn_3. The process may be kinetically slow enough to not finish during arc melting, as the SEM results for the annealed sample, described below, indicate.

Figure 9a and 9b show representative images for U-10Zr-4.3Sn-4.7Ln after annealing at 650 °C for 500 hours. Two types of precipitates remain after annealing, the Zr-Sn precipitates and the round Sn-Ln precipitates. The rough, random shaped precipitates shown in Figure 8b are no longer present, indicating the conversion of Zr_5Sn_3 to Ln_5Sn_3 is complete, or at least closer to completion. Higher magnification images with EDS points are shown in Figure 10. An expanded region from Figure 9a is shown in Figure 10a, while Figure 10b is an expanded region from

Figure 9b. The matrix region (points 1-6 in Figure 10a, Table 7) shows the separation of the matrix into α-U and δ phase, as observed in Figure 5 for U-10Zr-4.3Sn. The alloy with Ln has substantially more δ phase (visual observation), though, due to Zr no longer being consumed in Zr-Sn precipitates. There are still Zr-Sn precipitates present, though (points 7-9, Figure 10a, Table 7), due to the small molar excess of Sn (in relation to the lanthanides).

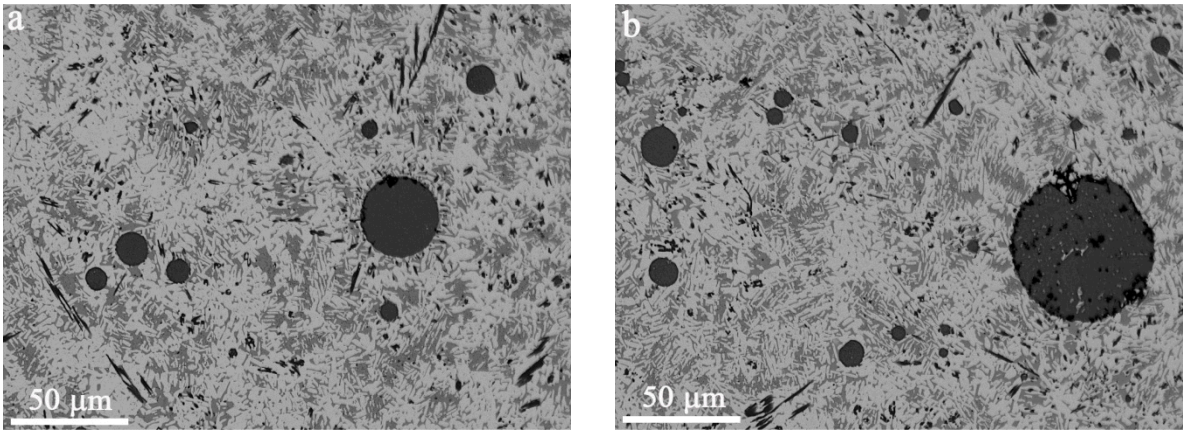

Figure 9. a. and b. SEM BSE images of annealed U-10Zr-4.3Sn-4.7Ln.

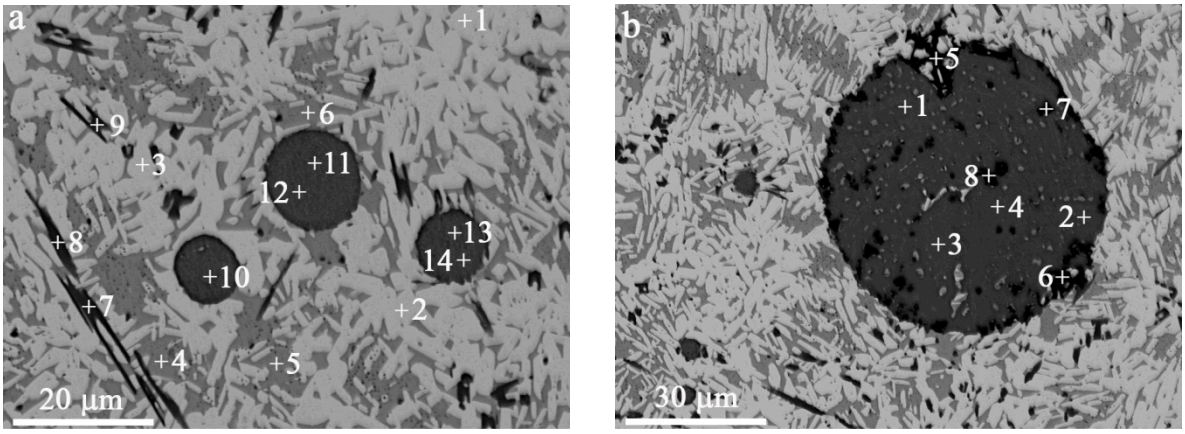

Figure 10. a. higher magnification region from image shown in Figure 9a; b. higher magnification region from image shown in Figure 9b. EDS data listed in Table 7.

Table 7. EDS data for points shown in Figure 10. Values in atomic %.

	U	Zr	Sn	Nd	Ce	Pr	La
Figure 10a							
1	96.9	0.7	1.5	0.0	0.2	0.6	0.0

2	97.9	0.6	1.2	0.0	0.1	0.2	0.0
3	97.3	0.7	1.7	0.0	0.0	0.3	0.0
4	38.3	60.0	0.8	0.0	0.5	0.2	0.3
5	37.5	59.9	2.0	0.0	0.4	0.1	0.1
6	38.5	59.8	1.1	0.0	0.3	0.1	0.1
7	3.8	59.4	34.4	1.6	0.5	0.3	0.0
8	5.9	58.7	32.9	1.6	0.4	0.4	0.0
9	6.0	58.5	32.7	1.4	0.7	0.6	0.1
10	1.9	11.5	36.2	22.0	18.4	8.3	1.8
11	1.8	15.1	36.2	21.6	15.7	7.7	1.9
12	1.9	15.9	35.5	21.7	15.5	7.7	1.9
13	2.2	15.0	36.3	21.4	15.7	7.7	1.7
14	2.2	14.9	35.7	21.1	16.5	7.8	1.7
Figure 10b							
1	1.6	9.5	36.8	24.6	16.1	8.6	2.7
2	2.4	11.3	36.3	24.7	14.6	8.3	2.5
3	1.6	10.0	37.1	25.8	14.6	8.8	2.1
4	1.9	10.4	37.0	25.8	14.2	8.5	2.2
5	3.5	95.4	0.6	0.1	0.2	0.1	0.1
6	1.6	96.0	1.2	0.7	0.3	0.3	0.0
7	1.6	89.5	4.5	2.0	1.5	0.7	0.2
8	1.4	93.2	2.9	1.3	0.7	0.5	0.1

In general, the smaller Sn-Ln precipitates, such as those shown in Figure 10a, are uniform in composition throughout, although a thin layer of Zr can be found around the periphery of the precipitate. EDS points 10-14 in Figure 10a and Table 7 are very consistent for 3 separate precipitates. The only measurable change is the variation in Zr and Ce. When Ce is slightly higher, Zr is slightly lower, as observed in point 10 in Figure 10a, Table 7, and point 1 in Figure 10b, Table 7. In all of the precipitates analyzed, roughly 10-15 at% Zr was present. Using points 10-14 in Figure 10a and points 1-4 in Figure 10b, Table 7, the Ln/Sn average ratio is 1.39, placing the composition between Ln_5Sn_4 and Ln_5Sn_3, but closer to Ln_5Sn_4. Including Zr with the lanthanides, the Ln+Zr/Sn average ratio is 1.70, very close to the Ln/Sn ratio of 1.67 for Ln_5Sn_3. The crystal structure for Zr_5Sn_3 is $P6_3/mcm$, prototype Mn_5Si_3. This is identical to the crystal structure for Nd_5Sn_3, and the high temperature crystal structures for Ce_5Sn_3, Pr_5Sn_3, and La_5Sn_3 [27][28][29]. Zr may be substituting into the lattice, replacing a small number of lanthanide

atoms to create $(Ln+Zr)_5Sn_3$. The transition from low temperature to high temperature structure, with a small amount of variation based on the lanthanide, occurs in the range of 400°C, so is easily accessible when arc melting during alloy fabrication. More importantly, this is below the operating temperature of a fast reactor, so if this substitution is taking place, it can occur under reactor conditions.

The role of Zr in the Ln-Sn precipitates is uncertain, but whether Zr is participating in the crystal structure or simply dissolved, the structures are lanthanide rich, even with a small molar excess of Sn in the alloy. The excess Sn is found primarily in Zr_5Sn_3 precipitates, with a small amount in the U-Zr matrix. Due to the favorable Ln/Sn molar ratio in the precipitates, there is a reserve of Sn available for higher Ln loadings. Based on the current alloy, 65.4U-21.1Zr-7.0Sn-6.5Ln at%, this amount of Sn could be expected to bind 11.6 at% Ln, without participation by Zr. The maximum Ln loading drops to 9.7 at% if Zr is included in the crystal structure. Using the lanthanide concentrations reported for 8% and 16% burn-up (2.8 and 5.6 at%, respectively) [3] and extrapolating, the current loading of Sn could bind all the lanthanides produced at a maximum burn-up of 33% (corresponding to 11.6 at% Ln).

Large precipitates, such as that shown in Figure 10b, have a mottled appearance. EDS analysis indicates the majority of the precipitate is Sn-Ln, while the black spots are Zr. The small white inclusions are likely trapped α-U. The concentration of Sn is roughly the same as for the small precipitates shown in Figure 10a, but the Zr content is slightly lower and the Ln content is slightly higher for each Ln constituent. The Ln+Zr/Sn ratio (average of points 1-4 in Figure 10b, Table 7) is 1.67, indicating the structure is still $(Ln+Zr)_5Sn_3$.

There is no direct correlation between the rough precipitate shown in Figure 8b and the precipitate shown in Figure 10b, due to the as-cast and annealed analysis being performed on

different sections of the pin. The large annealed precipitate likely came from a similar precipitate as that shown in Figure 8b, though, based on physical appearance. The Zr and U inclusions could be trapped, or the sample may not have been annealed for a long enough time to allow migration out of the precipitate. A Zr rind is present, as it is in the 3 smaller precipitates shown in Figure 10a. Small Zr precipitates are present around the large Ln precipitates, separate from the precipitate but close, but not throughout the bulk of the alloy. It appears that excess Zr is migrating out of the precipitates and slowly dissolving into the U-Zr matrix. As previously discussed, the conversion from Zr_5Sn_3 to Ln_5Sn_3, or some variation of $(Ln+Zr)_5Sn_3$, must be kinetically slow, thus annealing for 500 hours was not sufficient for the process to finish.

4. Conclusions

The data presented indicates Sn is a viable and possibly very good additive to control FCCI in a metallic fuel. Sn has been investigated as a small component in fuel cladding, but this is the first investigation of Sn as an additive to the fuel. The following conclusions can be drawn from the data presented:

- There is a clear preference for Sn to bind the lanthanides, releasing Zr back into the U-Zr matrix. The alloy containing lanthanides was fabricated starting with a U-Zr-Sn pre-alloy and adding lanthanides, thus the Zr-Sn precipitates had to break apart in order to form the Ln-Sn precipitates.
- In the current investigation, there was a small molar excess of Sn over the lanthanides, but the thermodynamically most stable Sn-Ln intermetallics formed, Ln_5Sn_4 and Ln_5Sn_3, even though the lanthanides were the limiting reagent. Further work is needed to determine if Ln_5Sn_3 (or $(Ln+Zr)_5Sn_3$) is the predominant structure, or if there is a mix of

intermetallics. That work is in progress, but regardless of the exact compound being formed, they are both Ln-rich. The significant consequence is that less Sn is required to bind the lanthanides than if a 1/1 compound or a Sn-rich compound was formed.

- When using a fuel additive, extra Zr will be needed to negate the removal of Zr from the matrix. Zr_5Sn_3 is the primary intermetallic being formed, possibly with some Zr_5Sn_4. Both compounds are Zr-rich, but the ratio of Zr to Sn is less than 2. Other additives, specifically In [6] and Pd [3], that have been investigated both have a Zr/additive ratio of 2 or more. The Zr/Pd ratio is 2, while the Zr/In ratio is 2.5, thus depleting a large amount of Zr from the U-Zr matrix. Of the 3 additives investigated, Sn will have the least impact on the fuel solidus and liquidus.
- Based on the above observations, Sn may be expected to outperform Pd, which outperforms Indium. Also, Sn is more abundant than In and Pd in the earth's crust, so less expensive for large scale fabrication. Sn is therefore recommended for irradiation testing.

Acknowledgments

The authors gratefully acknowledge the Department of Nuclear Energy, Office of Nuclear Energy, Science, and Technology, under DOE-NE Idaho Operations Office Contract DE-AC07-05ID14517.

References

[1] Keiser, D. D. "Fuel-Cladding Interaction Layers in Irradiated U-Zr and U-Pu-Zr Fuel Elements", Tech. Rep., Argonne National Laboratory-West (2006).

[2] W.J. Carmack, H.M. Chichester, D.L. Porter, D.W. Wootan, J. Nucl. Mater., 473 (2016) 167-177.

[3] R.D. Mariani, D.L. Porter, T.P O'Holleran, S.L. Hayes, J.R. Kennedy, J. Nucl. Mater., 419 (2011) 263-271.

[4] K.S. Lee, I.Y. Kim, W. Lee, Y.S. Yoon, Metals Mater., Intnl., 21 (2015) 498-503.

[5] W.Y. Lo, Y. Yang, J. Nucl. Mater., 451 (2014) 137-142.

[6] Y.S. Kim, T. Wiencek, E. O'Hare, J. Fortner, A. Wright, J.S. Cheon, B.O. Lee, J. Nucl. Mater., 484 (2017) 297-306.

[7] G.W. Egeland, R.D. Mariani, T. Hartmann, D.L. Porter, S.L. Hayes, J.R. Kennedy, J. Nucl. Mater., 440 (2013) 178-192.

[8] G.W. Egeland, R.D. Mariani, T. Hartmann, D.L. Porter, S.L. Hayes, J.R. Kennedy, J. Nucl. Mater., 432 (2013) 539-544.

[9] S.D. Herrmann, S. Li, Nucl. Tech. 171 (2010) 247-265.

[10] R. D. Mariani, D.L. Porter, S.L. Hayes, J.R. Kennedy, Metallic Fuels: The EBR-II legacy and recent advances, Ed. C. Poinssot, ATALANTE 2012, Nuclear Chemistry for Sustainable Fuel Cycles, 7, 513-520.

[11] S.K. Jha, N. Keskar, K.I. Vishnu Narayan, K.V. Mani Krishna, D. Srivastava, G.K. Dey, N. Saibaba, J. Nucl. Mater., 482 (2016) 12-18.

[12] N. Keskar, K.V. Mani Krishna, D. Srivastava, G.K. Dey, J. Nucl. Mater., 465 (2015) 71-77.

[13] S. Liu, Y. Zhan, J. Wu, X. Wei, J. Phys. Chem. Solids, 86 (2015) 177-185.

[14] J. Wang, K. Wang, C. Ma, L. Xie, J. Chem. Thermodynamics, 92 (2016) 158-167.

[15] A.K. Pattanaik, R. Kandan, K. Nagarajan, P.R. Vasudeva Rao, J. Alloys Comp., 551 (2013) 249-254.

[16] C.B. Basak, J. Nucl. Mater., 416 (2011) 280-287.

[17] Y.U. Kwon, J.D. Corbett, Chem. Mater., 2 (1990) 27-33

[18] J.T. McKeown, S. Irukuvarghula, S. Ahn, M.A. Wall, L.L. Hsiung, S. McDeavitt, P.E.A. Turchi, J. Nucl. Mater., 436 (2013) 100.

[19] R.I. Sheldon, E.M. Foltyn, D.E. Peterson, Sn-U (Tin-Uranium), Binary Alloy Phase Diagrams, II Ed., Ed. T.B. Massalski, 3 (1990) 3409-3410

[20] H. Okamoto, J. Phase Equilib., 14 (1993) 267-268

[21] S. Ahn, S. Irukuvarghula, S.M. McDeavitt, J. Alloys Comp., 611 (2014) 355-362.

[22] Monsanto Research Corporation, Reactor Fuels and Materials Development Plutonium Research: 1966 Annual Report (Mound Laboratory Report MLM-1402), Miamisburg, OH, 1967.

[23] D.E. Janney, T.P. O'Holleran, J. Nucl. Mater., 460 (2015) 13-15.

[24] I.P. Semitelou, J.K. Yakinthos, E. Roudaut, J. Magn. Magn. Mater., 128 (1993) 79-82.

[25] F. Weitzer, K. Hiebl, P. Rogl, J. Solid State Chem., 98 (1992) 291-300.

[26] M.T. Benson, unpublished data.

[27] G. Borzone, A. Borsese, R. Ferro, J. Less Common Met., 85 (1982) 195-203.

[28] G. Borzone, A. Borsese, R. Ferro, Z. Anorg. Allg. Chem., 501 (1983) 199-208.

[29] E. Franceschi, J. Less Common Met., 66 (1979) 175-181.